

**Indications of  $2\nu 2K$  capture in  $^{78}\text{Kr}$** Yu. M. Gavriluk, A. M. Gangapshev, V. V. Kazalov, and V. V. Kuzminov  
*Baksan Neutrino Observatory INR RAS, Russia*

S. I. Panasenko and S. S. Ratkevich\*

*V. N. Karazin Kharkiv National University, Kharkiv, Ukraine*

(Received 6 August 2012; published 4 March 2013)

Results from searches of double  $K$  capture in  $^{78}\text{Kr}$  in an experiment with the large-volume copper proportional counter, using data samples corresponding of two independent series of measurements with different intrinsic radioactivity background are presented. The total exposure of the low-background measurements is  $0.343 \text{ kg} \times \text{y}$ . A combination of methods of selection of useful events with a unique set of characteristics and wavelet analysis of events allowed a reduction of the background by  $\sim 2000$  times in the energy region of interest. The statistical significance of combined data from two stages of operation equals  $2.5\sigma$ . Corresponding to such effect, the half-life of  $^{78}\text{Kr}$  relative to  $2\nu 2K$  capture equals  $T_{1/2} = [9.2_{-2.6}^{+5.5}(\text{stat}) \pm 1.3(\text{syst})] \times 10^{21} \text{ y}$ . Half-life limits for other  $2K$  transitions to the excited states in  $^{78}\text{Se}$  are obtained at the level of  $10^{21} \text{ y}$  in the first time. In particular, limits on  $2\nu 2K$  capture to the excited level  $0_1^+$  (1499 keV) and resonant neutrinoless double  $K$  capture to the level  $2^+$  (2838 keV) have been defined on the level of  $T_{1/2} \geq 5.4 \times 10^{21} \text{ y}$  at 90% C.L.

DOI: [10.1103/PhysRevC.87.035501](https://doi.org/10.1103/PhysRevC.87.035501)

PACS number(s): 23.40.-s, 27.50.+e, 14.60.Pq, 21.10.Tg

**I. INTRODUCTION**

Most double- $\beta$ -decay investigations have focused on  $\beta^-\beta^-$  transition (two-neutrino-emitting and neutrinoless modes). This transition for the two-neutrino mode has been detected in direct and geochemical experiments for 11 nuclei, those of  $^{48}\text{Ca}$ ,  $^{76}\text{Ge}$ ,  $^{82}\text{Se}$ ,  $^{96}\text{Zr}$ ,  $^{100}\text{Mo}$ ,  $^{116}\text{Cd}$ ,  $^{128}\text{Te}$ ,  $^{130}\text{Te}$ ,  $^{150}\text{Nd}$ , and  $^{238}\text{U}$  (see review [1]), and in direct measurements of the  $2\nu\beta^-\beta^-$  decay half-life of  $^{136}\text{Xe}$ , recently reported by EXO-200 and KamLAND-Zen [2,3]. The data obtained for  $2\nu$  mode offer a chance to directly compare different models of the nuclear structure, which form the basis for calculations of nuclear matrix elements  $|M^{2\nu}|$ , and to select the optimal one.

Though direct correlation between the values of nuclear matrix elements for the two-neutrino and neutrinoless modes of double- $\beta$  decay is absent, the methods for calculating  $|M^{2\nu}|$  and  $|M^{0\nu}|$  are very similar, and a possibility to estimate their accuracy in calculating  $|M^{0\nu}|$  appears when comparing experimental data and theoretical calculations of  $2\nu\beta\beta$  decay probability. It may be expected that further accumulation of experimental data on the other types of  $\beta\beta$  processes [the decay with emission of two positrons ( $\beta^+\beta^+$ ), capture of bound atomic electrons with emission of a positron ( $\beta^+EC$ ), and double capture of two bound atomic electrons ( $ECEC$ )] will make it possible to considerably increase the quality of calculations for both  $2\nu$  and  $0\nu$  modes. Much effort is currently being made to search for these processes [4–8], in spite of the fact that the  $\beta^+\beta^+$  and  $\beta^+EC$  processes are strongly suppressed with regard to  $\beta^-\beta^-$  decay owing to the Coulomb barrier for positrons and a substantially lower kinetic energy of such transitions. Positrons are absent in the final state of the  $2\nu ECEC$  transition, and the kinetic energy of this transition could be rather high (up to 2.8 MeV), leading to a favorable

increase in the phase space and decay rate. However, this process is also hard to study for it could be detected only through its characteristic radiation. At present, a positive result was obtained only in a geochemical experiment with  $^{130}\text{Ba}$ , where the  $2\nu ECEC$  process was detected with a half-life of  $(2.2 \pm 0.5) \times 10^{21} \text{ y}$  [9].

The experiment to search for  $2K$  capture in  $^{78}\text{Kr}$  using a copper low-background proportional counter of large volume has been carried out at the Baksan Neutrino Observatory INR RAS since June 2005 [10]. The sensitivity ( $S$ ) of the setup with regard to half-life of  $2\nu 2K$  capture using data collected during 1 y of measurements was found to be  $S = 1 \times 10^{22} \text{ y}$ .

Different models give the following theoretical predictions (for the axial-factor coupling constant  $g_A = 1.254$ ) of  $^{78}\text{Kr}$  half-life for  $2\nu ECEC$  capture (see Table II):  $2.11 \times 10^{22} \text{ y}$  in the deformed shell model (DSM) [11],  $3.7 \times 10^{21} \text{ y}$  in the multiple commutator model (MCM) [12,13],  $3.7 \times 10^{22} \text{ y}$  in the quasiparticle random-phase approximation (QRPA) [14], and  $6.2 \times 10^{23} \text{ y}$  in the spin-isospin  $SU(4)_{\sigma\tau}$  symmetry [15]. The fraction of  $2\nu 2K$ -capture events in  $^{78}\text{Kr}$  with respect to the total number of  $2\nu ECEC$  events is 78.6% [16].

Comparison of experimental and theoretical values shows that sensitivity of measurements has passed the lower limit of theoretical calculations. This fact allows us to test the MCM [12,13].

The basic assumptions of the experiment to search for  $2K$  capture in  $^{78}\text{Kr}$  made in this work are described in Sec. II. Section III presents an experimental method and characteristics of detectors. The time-amplitude technique, the pulse-shape discrimination method, and a technique to separate single- and multipoint events and determine the charge in individual clusters in the counter are given in Sec. IV. Basic features of the digitized pulse processing using wavelet transform are also discussed in this section. Sections V and VI report the results of the background measurements for the large low-background proportional counter at the first and second

\* ratkevich@univer.kharkov.ua

stages, respectively. The combined results of these two stages of measurements are presented in Sec. VII. The conclusions are made in Sec. VIII.

## II. BASIC ASSUMPTIONS

When two electrons are captured from the  $K$  shell in  $^{78}\text{Kr}$ , a daughter atom of  $^{78}\text{Se}^{**}$  is formed with two vacancies in the  $K$  shell. Initially, the technique to search for this reaction is based on the assumption that the energies of characteristic photons and the probability that they will be emitted when a double vacancy is filled are the same as the respective values of the case when two single vacancies of the  $K$  shell in two singly ionized  $\text{Se}^*$  atoms are filled. In such a case, the total registered energy is  $2K_{ab} = 25.3$  keV, where  $K_{ab}$  is the binding energy of a  $K$  electron in a Se atom (12.65 keV). The fluorescence yield upon filling a single vacancy of the  $K$  shell in Se is 0.596. The energies and relative intensities of the characteristic lines in the  $K$  series are  $K_{\alpha 1} = 11.222$  keV (100%),  $K_{\alpha 2} = 11.181$  keV (52%),  $K_{\beta 1} = 12.496$  keV (21%), and  $K_{\beta 2} = 12.65$  keV (1%) [17]. The probability of deexcitation of a doubly ionized  $K$  shell through the emission of Auger electrons ( $e_a, e_a$ ) only, or through a single characteristic x ray and an Auger electron ( $K, e_a$ ), or through two characteristic x rays and low-energy Auger electrons ( $K, K, e_a$ ) is  $p_1 = 0.163$ ,  $p_2 = 0.482$ , and  $p_3 = 0.355$ , respectively. In a more refined description presented later in the paper, the energies and emission probabilities differ slightly from the above values.

A characteristic photon can pass a long distance in the gas from the point of its origin to the point of its absorption. For example, 10% of characteristic photons of 12.6 keV energy are absorbed on a length of 2.42 mm ( $P_{\text{gas}} \sim 4.36$  bar) [18]. Auger electrons of the same energy will be absorbed on a length of 0.44 mm, which produce almost pointwise charge clusters of primary ionization in the gas [19]. In the case of emission of two characteristic photons absorbed in a gas the energy release will be distributed between three pointwise regions. These events have a number of unique features and are the subject of study in this paper.

## III. EXPERIMENTAL TECHNIQUE

To register this process a large proportional counter (LPC) with a casing of M1-grade copper has been used. A LPC is a cylinder with inner and outer diameters of 140 and 150 mm, respectively. A gold-plated tungsten wire of 10  $\mu\text{m}$  in diameter is stretched along the LPC axis and is used as an anode. A potential of +2400 V is applied to the wire, and the casing (the cathode) is grounded. Both ends of the anode are electrically connected to the corresponding end-cap flanges via high-voltage pressure-sealed ceramic insulators with a central electrode taken from spark plugs.

To reduce the influence of the edges on the operating characteristics of the counter, the end segments of the wire are passed through the copper tubes (3 mm in diameter and 38.5 mm in length) electrically connected to the anode. Gas amplification is absent on these segments, and charge is collected in an ionization mode. Taking into account Teflon

TABLE I. Isotopic compositions of the krypton samples.

Samples, volume	Krypton isotopes					
	78	80	82	83	84	86
	Content (vol %)					
$^{78}\text{Kr}$ , 47.65 NL	99.810	0.170	0.005	0.005	0.005	0.005
$^{\text{depl}}\text{Kr}$ , 100 NL	0.002	0.411	41.355	58.229	0.003	–
$^{\text{nat}}\text{Kr}$	0.354	2.270	11.560	11.550	56.90	17.37

insulator dimensions, the distance from the operating region to the flange is 70 mm.

The length of the LPC operating volume is 595 mm (the distance between the butt ends of the tubes), and the LPC operating volume is 9.159 L. The total capacitance of the counter and outlet insulator is  $\sim 30.6$  pF. Indium wire is used to seal all detachable joints, and Teflon gaskets are used to seal all nipple joints. The inner insulators are made of Teflon, and their thickness was minimized to improve the degassing conditions during the vacuum treatment of the counter and to stabilize its operating characteristics.

The LPC was placed inside the shielding of 18-cm-thick copper, 15-cm-thick lead, and 8-cm-thick borated polyethylene layers. The installation is located in one of the chambers of the underground laboratory of the Gallium Germanium Neutrino Telescope experiment at the Baksan Neutrino Observatory, INR RAS, at a depth of 4700 mwe, where cosmic ray flux is lowered by  $\sim 10^7$  times down to the level of  $(3.03 \pm 0.10) \times 10^{-9} \text{ cm}^{-2} \text{ s}^{-1}$  [20].

The counter is filled with pure krypton gas up to 4.42 bar having no quenching or accelerating gaseous additions and is purified through a Ni/SiO<sub>2</sub> absorber (twice cleared) from electronegative admixtures. Two samples of krypton were used in this work: one of 48.6 L volume enriched in  $^{78}\text{Kr}$  up to 99.8% and natural krypton (100 L) left after  $^{78}\text{Kr}$  isotope extraction (depleted krypton) at normal temperature and pressure. Both samples have been specially cleared from radioactive isotope  $^{85}\text{Kr}$  ( $T_{1/2} = 10.756$  y), present in atmospheric krypton. The procedure for purifying an enriched sample was described in Ref. [21]. The final isotopic composition of the samples is listed in the Table I. The last row in the Table I shows the isotopic composition of the original natural krypton for comparison.

The detector signals are passed from one end of the anode wire to the charge-sensitive amplifier (CSA) attached to the high-voltage insulator through the capacitor. The CSA parameters have been optimized for transmission of a signal with minimum distortions, and information on the primary-ionization charge spatial distribution in its projection to the counter radius is fully represented in the pulse shape. After amplification in an auxiliary amplifier the pulses are collected by the LA-n20-12PCI digital oscilloscope. The oscilloscope, integrated with a personal computer, records the pulse wave form as the numerical vector digitized with a frequency of 6.25 MHz. The length of the scanning frame is 1024 and 2048 points at the first and second stages, respectively (163.8  $\mu\text{s}$ ),  $\sim 50$   $\mu\text{s}$  is the “prehistory” and  $\sim 114$   $\mu\text{s}$  is the “history”.

Processing of digitized pulses in “offline” mode is carried out using the technique developed in this work. This technique rejects pulses of no-ionized nature and allows one to exclude the procedure of taking signals from both ends of the anode wire, as was the case in Ref. [22], where this procedure was used to determine the coordinates of the event and eliminate pulses produced by microdischarges outside the operating length of the LPC from its amplitude spectra.

#### IV. IDENTIFICATION OF MULTIPOINT EVENTS

The response of a linear time-invariant system to some influence can be expressed by the convolution integral:

$$q(t) = \int_{-\infty}^{\infty} h(\tau)i(t - \tau)d\tau, \quad (1)$$

where in our case  $i(t)$  is the electric current at the output of the LPC,  $q(t)$  is the signal from the CSA, and  $h(t)$  is the pulse transitive characteristic of the CSA. To describe the output signal recorded by the digital oscilloscope in the form of a discrete set of instantaneous values of amplitudes one can move from integration to summation of instantaneous function values with a step  $\Delta t$ :

$$q(k\Delta t) = \Delta t \sum_n h(n\Delta t)i(k\Delta t - n\Delta t), \quad (2)$$

The pulse shape of registered charged particles (or photons) taken from the LPC has some definite features that allow us to easily distinguish them from nonionized noise signals and microdischarge events. The registered events, in their turn, can be sorted out as “pointlike” and “lengthy” events by comparing their pulse rise time. Pointlike pulses with a small rise time for the pulse front are produced by particles which interact with a krypton gas in the counter in some particular region whose characteristic length is small in comparison with the cathode radius. Long-duration, complex events can be produced when several pointlike events are simultaneously registered at different distances from the anode (“multipoint” or “multicluster” events). Besides, “extended” pulses arise in a case when the fast electron track length is commensurate with counter radius.

Idealized pulse shape events taken at the output of the LPC and charge pulses taken from the CSA’s output produced by single-point events are shown in Fig. 1. The derivative of a pulse taken from the CSA replicates the shape of an electric current signal from the LPC’s anode wire. In a simplified case one can calculate the value of current in the LPC by

$$\bar{i}_n = \frac{\bar{q}_n - \bar{q}_{(n-1)}}{\Delta t}, \quad (3)$$

where  $\Delta t = t_n - t_{n-1}$ .

A pulse taken from the anode wire is formed mainly owing to the negative charge induced onto the anode by positive ions moving towards the cathode and which was produced near the wire during the gas amplification (ionic component, i.c.). The contribution of the charge induced at the anode by electrons from avalanches (electronic component, e.c.) is small enough because they have to pass a small potential

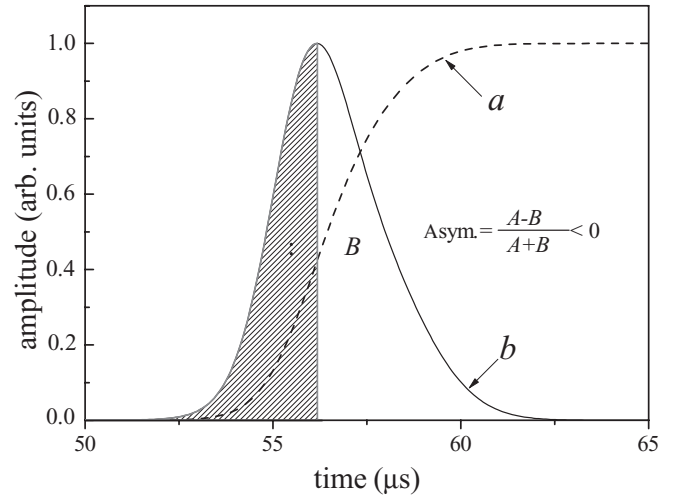


FIG. 1. A depiction of idealized pulse shape single-point event from the LPC. The monotonically dashed curve  $a$  is a charge pulse from the CSA output, and the front-back asymmetric solid curve  $b$  is an electric current pulse (constructed by differentiating the charge pulse).  $A$  and  $B$  denote the area in the front and back halves of the midpoint of the current pulse, respectively.

difference on their way to the anode. The electric current pulse shape is affected by the distribution in the density of primary ionization electrons crossing the border of the gas amplification region. The distribution parameters depend on drift time of the originally pointlike charge towards the anode. The pointlike ionization is smeared out during the drift time owing to diffusion of the electrons into a cloud with a radial charge density distribution that is close to Gaussian.

As is seen in Fig. 1, the electric current signal produced as a result of gas amplification has an asymmetric form and cannot be described by a single Gaussian curve. The values of  $A$  and  $B$  (Fig. 1) are the area in the front and back halves of the midpoint of the current pulse, respectively. There is a mathematical procedure that allows conversion from a registered charge pulse to an electric current pulse produced by primary ionization electrons through the boundary of the avalanche region. A detailed description of the algorithm for electronic component segregation is given in Ref. [23]. The obtained form of a signal can be described by a set of Gaussian curves, thus determining the charge that was deposited in separate components of a multipoint event. The calculated area of an individual Gaussian should correspond to the charge (energy) of the corresponding pointlike ionization.

Figure 2 illustrates a demo version of a shape of an electric current pulse  $i(t)$ : (a) from the LPC and the corresponding CSA pulse (b) from a three-point event expected from  $2K$  capture in a case of registering two characteristic x-rays and a cascade of low-energy Auger electrons.

In Fig. 2, in addition to the primary pulse, there is a secondary pulse, smaller in amplitude, owing to the photoelectrons knocked out of the copper case by photons produced in the electronic avalanches in the gas amplification process.

Photoeffect on the cathode is probable enough because of the absence of quenching additions in the krypton gas. The delay between pulse and after-pulse is determined by the total

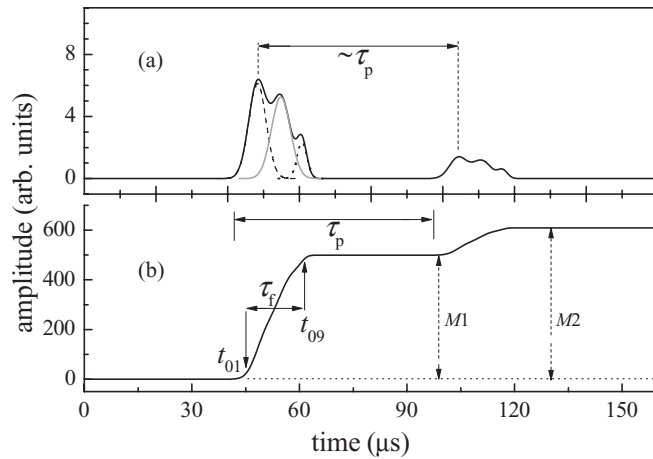


FIG. 2. A depiction of idealized pulse shape analysis parameters from three-point event expected from  $2K$  capture in case of registering two characteristic photons and a cascade of low-energy Auger electrons from the LPC: (a) the electric current pulse, (b) the charge pulse.  $t_{01}$  and  $t_{09}$  are the baseline plus 10% and 90%, respectively, of the pulse height;  $\tau_r = t_{09} - t_{01}$  is the pulse rise time;  $\tau_p$  is the time of the after-pulse appearance since the beginning of the primary pulse.

drift time of the electrons to move from the cathode to the anode. It presets the duration of the time interval to allocate totally any single event regardless of its primary ionization distribution over the LPC volume. In case of pure krypton the calculated drift time for the ionization electrons to move from the cathode to the anode is  $58 \mu\text{s}$ . A Gaussian area or a sum of Gaussians in the case of a multipoint event for an interval of  $58 \mu\text{s}$ , starting from the beginning of a pulse, gives total number of primary ionization electrons.

For the pulse shape analysis we have used the following signal parameters indicated in Fig. 2: (1)  $\tau_r = t_{09} - t_{01}$  is the pulse rise time, where  $t_{01}$  and  $t_{09}$  are the moments where the pulse amplitude has reached 10% and 90%, respectively, of its maximum value  $M1$ ; (2)  $\tau_p$  is the time of the after-pulse appearance since the beginning of the primary pulse; (3)  $\lambda$  distribution,

$$\lambda = (M2 - M1)/M1, \quad (4)$$

is the ratio of the difference between the after-pulse's and primary pulse's maximum amplitudes to the primary pulse amplitude.

The parameters border corresponding regions where useful signals are expected and are determined from the distribution plotted for the pulses with known characteristics obtained from the calibration sources [24]. Using these boundaries we select the candidate events for  $2K$  capture from the whole set of events registered in the course of basic measurements.

Figures 3(a) and 3(b) show converted pulses of voltage (charge) normalized for  $M1$  of an original CSA pulse and obtained by integrating electric current pulses owing to primary ionization electrons [Figs. 3(c) and 3(d)] from two real events which are candidates for  $2K$  capture of  $^{78}\text{Kr}$ .

As seen in Figs. 3(c) and 3(d), the electric current pulses are very noisy. Noise and possible electrically induced signals can

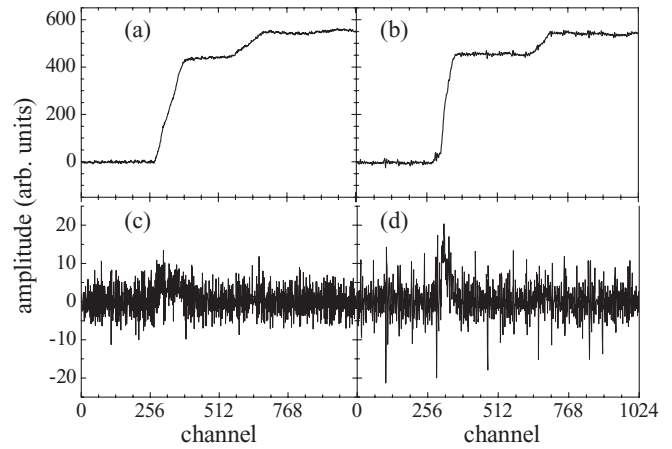


FIG. 3. (a) and (b) curves demonstrate the converted pulses of voltage (charge) normalized for  $M1$  of an original CSA pulse and obtained by integrating electric current pulses owing to primary ionization electrons (c) and (d) from two real events which are candidates for  $2K$  capture of  $^{78}\text{Kr}$ .

both mask the low-energy component and produce a false one. Smoothing procedures were applied to the initial pulse, with a following differentiation of it, resulting in deterioration of electric current pulse resolution. Traditional frequency filtering methods with various window functions, such as filters of Hamming, Winner, Sawitsky-Golay, and others [23], applied to the electric current signal do not allow one to always separate with enough reliability closely located other components of a compound event that are masking each other.

#### A. Useful signal extraction from noisy LPC electric current pulses with wavelet analysis

At present the mathematical base for wavelet analysis is well developed and presents a good alternative to the Fourier transform in studying time (spatial) series with distinct irregularity. Wavelet transform, for a one-dimensional signal in particular, consists in its decomposition, through zooming and translations, on a basis constructed from a wavelike oscillation function with definite properties called wavelet. Each function of this basis is characterized both by a definite spatial (time) frequency and its localization in the physical space (time). The localized basis functions of wavelet transform resemble the signals under investigation to a greater degree than the Fourier basis functions.

Thus, the distinction between the Fourier transform, conventionally used for signal analysis, and the wavelet transform is that the latter provides a two-dimensional evolvent of the investigated one-dimensional signal where frequency and coordinate are considered to be independent variables, which means that in the wavelet transform an increase in resolution of one of these variables does not automatically result in the decrease of resolution of the other. This independence of both variables allows one to simultaneously analyze the properties of a signal in both physical (time, coordinate) and frequency spaces [25,26]. The wavelet transform has also a distinction from the short-time Fourier transform (the Gabor

transform) that also results in a two-dimensional spectrum. The distinction is that one and the same function constitutes the basis of the former while in the case of the latter the functions are different [25], and thus the wavelet transform provides the better time-frequency localization, flexibility of analysis, and possibility to choose the best-fitting form of the wavelet function.

For our application, the extraction of a real signal from noisy data is better approached with the mathematical tool of the discrete wavelet transform (DWT). The DWT algorithm is based on a discrete signal vector  $\{f(n)|n \in N\}$  for which a wavelet spectrum is calculated, which in turn is also a discrete vector. Orthonormal bases on a binary lattice exist for which algorithms of multiresolution analysis (MRA) or multiscale approximation (MSA) have been developed [27].

The idea of the latter consists of representing a signal by a sequence of images with a different degree of detailing. Each image contains independent nonoverlapping information about a signal in the form of wavelet coefficients which are easily calculated by the iteration procedure known as fast wavelet transform. Taken as a whole, they solve the problem of the total analysis of a signal and substantially simplify diagnostics of the underlying processes.

MRA application allows one to represent the signal under investigation,  $\tilde{x}(n)$ , in the form of decomposition:

$$x^J(n) = \sum_{m=0}^{N_{j_0}-1} \tilde{a}_{j_0,m} \varphi_{j_0,m}(n) + \sum_{j=j_0}^J \sum_{m=0}^{N_j-1} \tilde{d}_{j,m} \psi_{j,m}(n),$$

where the first term is a rough approximation of the signal and the second adds refinements to the very high resolution at higher zoom levels,  $J$ ;  $\tilde{a}_{j_0,m} = \langle \tilde{x}, \varphi_{j_0,m} \rangle$  are empirical approximation coefficients and  $\tilde{d}_{j,m} = \langle \tilde{x}, \psi_{j,m} \rangle$  are empirical detail coefficients ( $\langle \cdot \cdot \cdot \rangle$  denotes the dot product);  $j, m \in \mathbb{Z}$  are the current values of scale and shift;  $N_j$  ( $N_j$ ) is the number of approximation coefficients (detail coefficients) considered at the corresponding levels of decomposition;  $j_0$  is the initial scale value;  $J$  is the final scale value.

Parameter  $J$  specifies the resolution of wavelet reconstruction  $x^J(n)$  of original signal  $\tilde{x}(n)$ . Actually, in the case of tendency  $J \rightarrow \infty$ , the norm tends to  $\|x^J - \tilde{x}\| \rightarrow 0$ .

The primal father function (scaling functions) is defined as the solution of the homogeneous scaling equation

$$\varphi(n) = \sqrt{2} \sum_{i=0}^{2K-1} h(i) \varphi(2n - i),$$

with normalization

$$\int \varphi(n) dn = 1.$$

The primal mother function is defined in terms of the father by a similar scaling equation,

$$\psi(n) = \sqrt{2} \sum_{i=0}^{2K-1} g(i) \varphi(2n - i),$$

where  $g(i) = (-1)^i h(2K - i - 1)$ . The parameter  $K$  is the order of the wavelet and the  $h(i)$  are a unique set of numerical

coefficients that satisfy certain relations such as orthogonality of basis functions [25,28].

All the properties of a wavelet basis are determined by the so-called filter coefficients  $h(i)$  [25]. A sufficiently detailed description of the preparation of the coefficients  $h(i)$  is considered in Refs. [26,29].

The discrete orthogonal wavelet transform at MRA can be defined as a recursive algorithm:

$$a_{(j-1),m} = \sum_{k \in N} h_{k-2m} a_{jk},$$

$$d_{(j-1),m} = \sum_{k \in N} (-1)^k g_{-k-2m+1} a_{jk}, \quad a_0 = \tilde{x}.$$

According to the Mallat pyramid algorithm [30], the initial signal is first passed through the decomposition filters of low and high frequency. The next step is to obtain approximation coefficients  $\tilde{a}_{j,m}$  at the output of the low-frequency filter and detail coefficients  $\tilde{d}_{j,m}$  at the output of the high-frequency filter, using decimation  $\downarrow 2$ . This algorithm goes on according to the scheme given below until it reaches the decomposition level  $J$ . In terms of wavelet coefficients the wavelet decomposition of a signal is presented in the following way.

$$W(\tilde{x}) = \tilde{a}_0 \rightarrow \{\tilde{a}_1, \tilde{d}_1\} \rightarrow \{\tilde{a}_2, \tilde{d}_2, \tilde{d}_1\} \rightarrow \dots$$

$$\dots \rightarrow \{\tilde{a}_N, \tilde{d}_N, \tilde{d}_{N-1}, \dots, \tilde{d}_1\}.$$

The solution of the noise-reduction problem is carried out in four steps: (1) the initial signal is decomposed; (2) the threshold value for noise is chosen for each level of decomposition; (3) the threshold filtration of detail coefficients is carried out; (4) the signal is reconstructed.

This technique is a nonparametric estimation of a regression model of a signal using an orthogonal basis [31,32] and works best for signals whose decomposition has a small amount of detail coefficients considerably different from zero.

The reconstruction of a function  $x(n)$  is carried out using the modified wavelet coefficients for the signal deconvolution:

$$\hat{x}(n) = \sum_{m=0}^{N_{j_0}-1} \hat{a}_{j_0,m} \varphi_{j_0,m}(n) + \sum_{j=j_0}^J \sum_{m=0}^{N_j-1} \hat{d}_{j,m} \psi_{j,m}(n), \quad (5)$$

where  $\hat{a}_{j_0,m}$  and  $\hat{d}_{j,m}$  coefficients passed wavelet thresholding.

As a rule, the criterion of entropy minimum ( $H$ ) is used to choose the optimum wavelet decomposition, being a logarithm of a signal's energy  $H = \sum \log(\hat{x}^2)$ .

The entropy of an initial signal reaches its maximum owing to the noisiness of a signal. With the increase of the wavelet decomposition the entropy decreases to its minimum, which corresponds to the optimal level of wavelet decomposition of the initial signal.

## B. Determination of the optimal noise reduction for a signal from the LPC

When studying the effects constituting a small fraction of the background one should, apart from the high quality of experimental data, impose high requirements for their processing. Setting of the input parameters for the arbitrary

noisy signals can present some difficulties in our case owing to the necessity of having *a priori* data or an analysis of statistical characteristics of high-frequency components of the signals. Because in the typical double- $\beta$  decay measurements (thousands of hours) the spectrum of noise can be exposed to substantial changes owing to possible electronic noise pickups and microphonic noise, some adaptive method of noise reduction is needed to minimize the uncertainty of the initial signal shape evaluation, which substantially influences the determination of the type of event.

It should be remarked that the choice of both a wavelet to be used and a level of decomposition depends on the properties of the signal under investigation. The smoother the wavelets, the smoother is the approximation of a signal. Conversely, sharper wavelets trace the peaks of an approximated function better. The level of decomposition affects the scale of sifted-out details. With the increase of the level of decomposition the model subtracts the increasing level of the noise, with the result that possible smoothing occurs not only of the noise but also of some local characteristics of a signal. A series of approximation and detail wavelet coefficients is needed for the wavelet transform.

The noisy component of a signal in most cases is reflected in the detail coefficients  $\tilde{d}_{j,m}$ , and these are the coefficients that are subject to processing in the noise-reduction technique. The noisy component, as a rule, has an absolute amplitude value less than that of the basic signal. So to reduce the noise one should zero those coefficients that are less than some threshold value. The choice of the threshold level of noise affects the quality of the signal noise reduction, which could be evaluated as a signal-to-noise ratio ( $P$ ):

$$P = \frac{\frac{1}{N_s} \sum_{n=1}^{N_s} s^2(n)}{\frac{1}{N_z} \sum_{n=1}^{N_z} (z(n) - \overline{z(n)})^2},$$

where  $s(n)$  and  $z(n)$  are the discrete vectors of a signal and noise; while  $N_s$  and  $N_z$  are their lengths, respectively.

Setting a small threshold keeps a residual noise in the detail coefficients and results only in insignificant increase in the signal-to-noise ratio. With a large-enough threshold one can lose coefficients carrying essential information. The search for an optimum threshold amounts to finding the maximum value of the signal-to-noise ratio with the least quadratic deviation of the estimated signal.

Let us express the empirical detail coefficients  $\{\tilde{d}_{j,m} | m \in [1, N_j]\}$  corresponding to level  $j$  by the linear relation

$$\tilde{d}_{j,m} = g_{j,m} + \sigma_j \vartheta_{j,m}, \quad (6)$$

where  $\{g_{j,m} | m \in [1, N_j]\}$  are the true detail coefficients of a signal without noise ( $N_j$  in this case is the number of detail coefficients, considered at a decomposition level  $j$ ), and  $\{\vartheta_{j,m} | \vartheta_{j,m} \in \text{norm}(0, \sigma_j^2), m \in [1, N_j]\}$  are the reading of the additive Gaussian noise with zero mean and variance,  $\sigma_j^2$ . Then the solution to the noise-reduction problem could be reduced to the search of estimates  $\{\hat{g}_{j,m} | m \in [1, N_j]\}$  of true detail coefficients:  $g_{j,m} = T(\tilde{d}_{j,m})$ . Such an estimate, carried out on the basis of empirical coefficients  $\{\tilde{d}_{j,m} | m \in [1, N_j]\}$  and a given threshold  $\theta_{j,i}$ , is, in fact, a construction of a regression

model of the true coefficients:

$$\hat{g}_{j,m} = d_{j,m} + \phi(d_{j,m}, \theta_{j,i}), \quad (7)$$

where  $\phi(d_{j,m}, \theta_{j,i})$  is the remainder term of thresholding function written in a general form. Expressing by the least-squares procedure the deviation of coefficients in the regression model (7) as some risk function

$$R_j(\theta_{j,i}) = \sum_{k=1}^{K_j} (\hat{g}_{j,k} - g_{j,k})^2, \quad (8)$$

where  $i \in N$ , we learn that the optimum value of the threshold  $\bar{\theta}_j$ , producing in accordance with the Stein criterion [33] the best noise reduction of a signal, corresponds to the case where function (8) has a global extremum:

$$\bar{\theta}_j = \arg \min_{\theta_{j,i} | i \in N} R_j(\theta_{j,i}).$$

To meet this criterion used in the noise reduction we applied the Birgé-Massart technique [34] to determine the threshold  $\bar{\theta}_j$  to treat the detail wavelet coefficients. Coefficients  $\tilde{d}_{j,m}$  less than the chosen threshold were zeroed while the others were diminished by  $\bar{\theta}_j$ . The optimum value of criterion  $\bar{\theta}_j$  has been chosen in accordance with minimum “entropy logarithm of signal energy” principle.

To enhance the reliability of both empirical signal shape determination and its parameters’ extraction we can add to each initial frame of a noisy pulse a known model signal with preset parameters and then process it with wavelet analysis. As a rule, during first  $\sim 40 \mu\text{s}$  (“prehistory”) in the frame of digitized pulse from the CSA [see Figs. 3(c) and 3(d)], there is a noise path only. In this interval of time we can select a vector of values containing no signal. Thus, we can produce a sampling control  $\{\tilde{z}(n) | n = 1, \dots, N_x/4; n = 1, \dots, N_x/4\}$  being equal to prehistory ( $N_x$  is the total length of the frame). We add a model signal  $s_o(n)$ , composed of three Gaussian curves summed together. We derive a model signal with a real noise having put in linear dependence of a width and center of the Gaussian curves on the rise time of the CSA output pulse,

$$\tilde{s}(n) = s_o(n) + \tilde{z}(n), \quad n = 1, \dots, N_x/4. \quad (9)$$

To find the optimum technique for noise reduction of a similar signal and to define a quantitative measure of concordance between the estimated  $\hat{s}(n)$  and initial  $s_o(n)$  signals, we introduce the following criteria:

$$A = \frac{\sum_{n=1}^N [\hat{s}(n) - s_o(n)]^2}{\sum_{n=1}^N s_o^2(n)}; \quad B = \frac{\sum_{n=1}^N \hat{s}(n)s_o(n)}{\sum_{n=1}^N s_o^2(n)}; \quad (10)$$

$$C = \sqrt{A^2 + (B - 1)^2}. \quad (11)$$

The minimum value of functional  $A$  corresponds to the identity of the estimated and modeling signals, and its maximum corresponds to their total anticorrelation. In contrast, the minimum value of functional  $B$  indicates the anticorrelation of the mentioned signals and its maximum standing for their total identity. So, the lesser  $A$  and greater  $B$ , the more accurate is the resurrection of a signal under investigation. In other words, the algorithm of the signal  $s_o(n)$  reconstruction

amounts to minimization of functional  $A(\hat{s})$  with simultaneous maximization of functional  $B(\hat{s})$ . The normalization of the introduced functionals allows comparing of various signals' decomposition for different wavelet function basis irrespective of the parameters of the signals and basic functions. Functional  $C(\hat{s})$  is a nonlinear combination of functional  $A(\hat{s})$  and functional  $B(\hat{s})$  and serves as a generalized quantitative characteristic of a quality of the reconstructed signal and is to be minimized.

### C. Detection of a signal against additive noises

The current task can be solved with MATLAB using the Wavelet Toolbox [35] for signal and image treatment. To choose the optimal wavelet allowing one to obtain the best of wavelet threshold of a signal, the criterion of maximum ratio of initial entropy ( $H_0$ ) and that purified from the noise signal ( $H$ ) was used:

$$\eta = H_0/H. \quad (12)$$

At the first stage we have selected the best "tree" for each type of wavelets using the criterion "entropy - logarithm of energy." The following orthogonal wavelets with compact carrier were used: Dobeshies (db $N$ ), Simlet (sym $N$ ) and Coiflet (coif $N$ ), where  $N$  is the index number, designating the number of nonzero coefficients in filters. Wavelets are not symmetrical and are not periodic enough. Simlet wavelets are close to symmetric to certain degree.

For each specified empirical signal we defined the optimal number of decomposition levels using numerical simulation for the case when the signal is resurrected to a large degree and the noise interference is not so large yet as to significantly distort the shape of a signal. The procedure of the signal resurrection is shown in Fig. 4 for the model signal  $s_o$ , which has additively added noise interference  $z_o$  taken from a real signal  $\tilde{x}(n)$ . As one would expect, both the quality of the estimated signal and the noise-to-signal ratio depend on the degree of overlapping of the wavelet spectra of a signal to be reconstructed and noisy signal.

After choosing the best wavelet for a given pulse using the entropy criterion, the functionals (10) and (11) for each level of wavelet decomposition have been calculated for different values of threshold criterion of noise purification. Values of  $H$ ,  $A$ ,  $B$ , and  $C$  are presented in Fig. 4 in (e), (f), (g) and (h), respectively, for eight levels of pulse wavelet decomposition of  $\tilde{s}(n)$  [Fig. 4(a)] using wavelet of Simlet sym8 and soft thresholding [36]. In soft thresholding one replaces  $\hat{d}_{j,m}$  in Eq.(5) with

$$\hat{d}_{j,m}^S = \text{sgn}(\hat{d}_{j,m})(|\hat{d}_{j,m}| - \theta_{\text{th}})I(|\hat{d}_{j,m}| > \theta_{\text{th}}),$$

where  $\theta_{\text{th}} > 0$  is a certain threshold.

Analysis of Figs. 4(b)–4(d) allows one to observe the change in the estimated signal with increase in number of decomposition levels  $L$  taken into account. Figure 4(c) shows that for decomposition level  $L = 4$  of a noise signal  $\tilde{s}(n)$  the minimum of functional  $C(\hat{s})$  corresponds to the maximum accuracy in model signal  $s_o(n)$ . With the decomposition level of  $L = 3$  we obtain the significant increase in sinusoidal

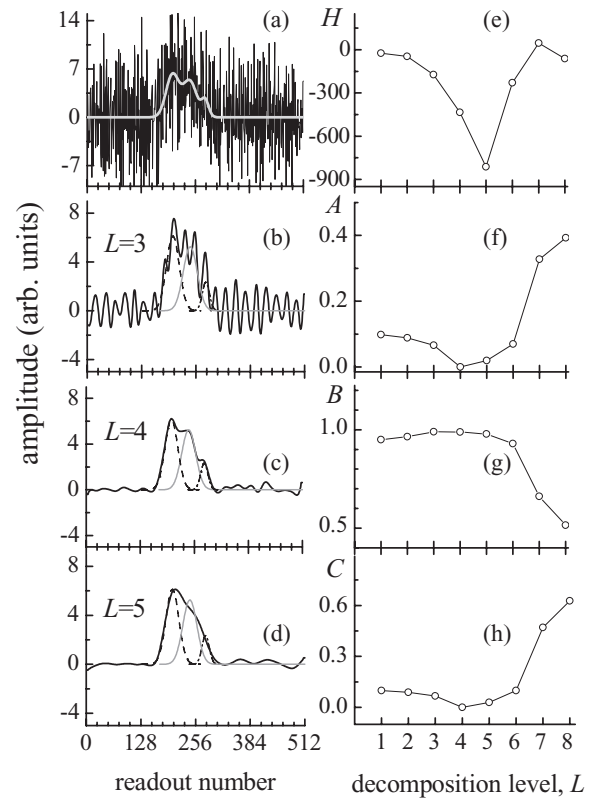


FIG. 4. Signal modeling graphs with the added real noise (a) and denoise of signals for various levels of decomposition: (b)  $L = 3$ , (c)  $L = 4$ , and (d)  $L = 5$ . (e) and (f), (g), (h) dependency's of entropy  $H$  and coefficients  $A$ ,  $B$ ,  $C$  from wavelet decomposition level, respectively.

noise, in case of ( $L = 5$ ), which corresponds to the minimum of entropy  $H$ , the estimated signal takes a smoother shape, resulting in stronger distortions of the initial model signal parameters.

Information on the type of event is contained in the shape of a electric current signal. Therefore the minimum of the functional  $C(\hat{s})$  serves in our case as a quantitative criterion for when an initial modeling signal without noise most closely describes the estimated signal.

Thus, by determining, with the help of a model signal with definite empirical noise, the depth of the wavelet decomposition and threshold values  $\theta_j$  for each decomposition level we find the resurrected empirical signal proper to the event in the LPC. By describing signals purified from noise with the help of a set of Gaussian curves using the minimization root-mean-square error technique one can separate multipoint events from single-point ones.

## V. RESULTS OF THE FIRST STAGE OF MEASUREMENTS USING THE LPC

Figure 5(a) shows the total spectra of  $M1$  amplitudes, normalized for 1000 h, obtained for the background of the LPC filled with krypton enriched in  $^{78}\text{Kr}$  (total collection time is 8400 h; spectrum 1, dark line), and with depleted krypton (total

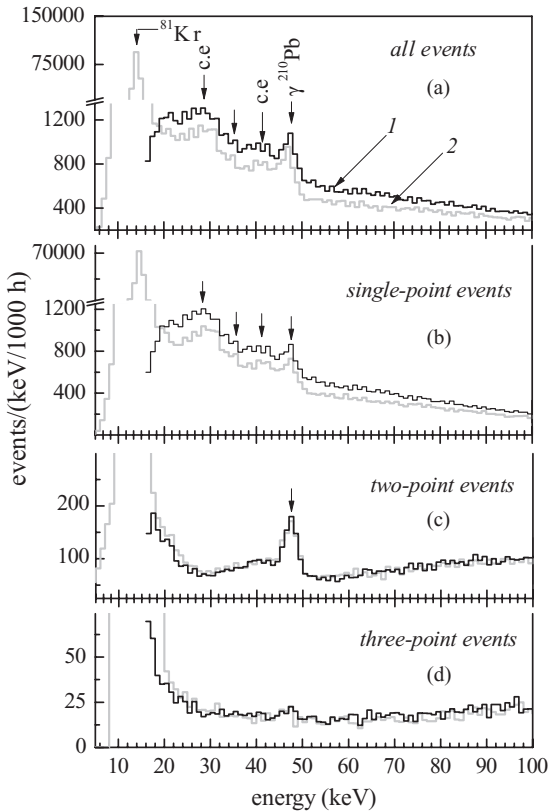


FIG. 5. Pulse-height  $M1$  spectra (data of the first stage of measurements normalized for 1000 h) of the background of the LPC filled with krypton enriched in  $^{78}\text{Kr}$  (1, dark line) and with depleted krypton (2, light line): (a) all events, (b) single-point events, (c) two-point events, and (d) three-point events.

collection time is 5000 h; spectrum 2, light line). Comparison of these spectra shows that the background of the counter filled with krypton enriched in  $^{78}\text{Kr}$  exceeds the background with depleted krypton at energy  $\geq 18$  keV. The shape of difference (subtracted) spectrum in the range of 20–100 keV is described reasonably well by the model spectrum composed of  $\beta$  spectra owing to  $^{85}\text{Kr}$  and  $^{14}\text{C}$  decay in the proportion 1:17. Background counting rates in this range are  $56.3\text{ h}^{-1}$  and  $47.2\text{ h}^{-1}$  when filled with  $^{78}\text{Kr}$  and  $^{\text{depl}}\text{Kr}$ , respectively. The difference in  $^{85}\text{Kr}$  isotope activities in the samples is attributable to its different residual value achieved during the isotopic purification.  $^{14}\text{C}$  isotope comes into the krypton gas during the continuous usage of the counter, supposedly as a result of slow sublimation of organic molecules (ethyl alcohol and acetone were used to clean the components when assembling the detector) from the surface of the body of the counter. Overactivity of  $^{14}\text{C}$  in the enriched krypton is attributable to the fact that this sample was measured first and the main portion of this organic vapor penetrated into it. Actually, all the events in the operating energy range produced by  $\beta$ -particle absorption can be considered as single-point ones, except for those events where  $\beta$  particles have lost their energy partially by generating bremsstrahlung.

At energies  $\leq 18$  keV, the counting rate of events in spectrum 2 is much higher than in spectrum 1. This is

attributable to the presence, in the original atmospheric krypton, of cosmogenic radioactive isotope  $^{81}\text{Kr}$  ( $T_{1/2} = 2.29 \times 10^5\text{ y}$ ) [37] with volume activity of  $\sim 0.1\text{ min}^{-1}\text{ L}^{-1}\text{ Kr}$  [38,39], the significant part of which comes into the sample of depleted krypton during the process of its production.  $^{81}\text{Kr}$  decays by electron capture, producing  $^{81}\text{Br}$  ( $K$  capture 87.5% [40]).  $K$  capture yields a 13.5-keV energy release. One can see the peak of this line in spectrum 2 (light line in Fig. 5). The resolution of the peak (FWHM) is 15.3%. Counting rate of events in the  $(13.5 \pm 3.0)\text{-keV}$  energy range is  $220\text{ h}^{-1}$ , which corresponds to a volume activity of  $^{81}\text{Kr}$   $(0.10 \pm 0.01)\text{ min}^{-1}\text{ L}^{-1}\text{ Kr}$ .

The filling of the  $K$ -shell vacancy of a daughter atom of bromine in 61.4% of decays is accompanied by the emission of characteristic x rays of 11.92 keV ( $K_{\alpha 1}$ , 100%), 11.88 keV ( $K_{\alpha 2}$ , 51.9%), 13.29 keV ( $K_{\beta 1}$ , 13.6%), and 13.47 keV ( $K_{\beta 2}$ , 1.36%) energies [37] and, accompanying them, Auger electrons of 1.55, 1.60, 0.27, and 0.01 keV, respectively (relative intensities of  $K_{\alpha\beta}$  lines are given in parentheses). Thus, it is clear that in the case of photon emission  $K_{\alpha 1}$ ,  $K_{\alpha 2}$  energy of Auger electrons is large enough to produce a distinct two-point event. Of all the events, 38.6% are attributable to the filling of the Br atom  $K$ -shell vacancy accompanied by a cascade of Auger electrons and are considered as events producing one-point energy release. Events with the emission of characteristic x rays  $K_{\beta 1}$  and  $K_{\beta 2}$  are also considered as one-point events because the energy release of Auger electrons does not exceed the CSA noise. Using the above data and taking into account the efficiency of characteristic x-ray absorption in a krypton gas of the LPC ( $\varepsilon_p = 0.869$ ), one can calculate the component composition of complete absorption peak with energy 13.5 keV with 49.4% single-point + 50.6% two-point event [23].

At 46.5 keV, in spectra 1 and 2 [Fig. 5(a)], one can see the peak corresponding to the source of  $^{210}\text{Pb}$  ( $T_{1/2} = 22.2\text{ y}$ ,  $\beta$  decay,  $E_\gamma = 46.5\text{ keV}$ , with a yield is 4.25% per decay [37]). The  $^{210}\text{Pb}$  isotope is produced after  $^{222}\text{Rn}$  ( $T_{1/2} = 3.82\text{ days}$ ,  $\alpha$  decay) in the  $^{238}\text{U}$  decay chain. It can be produced directly in copper material owing to trace radioactive contaminant decay (volume source) or accumulate on the surface of the case of the counter in the form of daughter isotopes of  $^{222}\text{Rn}$  decay,  $^{222}\text{Rn}$  being present in the atmospheric air (surface source), during the assembling of the detector.  $\gamma$  radiation comes into a fiducial volume of the counter from both sources. There are mainly single-point events (owing to the photoeffect on krypton with deexcitation owing to Auger electrons) and two-point events (owing to the photoeffect with the emission of krypton characteristic radiation) in the peak line of 46.5 keV, and only a small portion of events will be regarded as three-point ones where the primary photon or characteristic photon absorption occurred through the scattering on the outer electrons with the following absorption of the secondary quantum.

Conversion electrons (c.e.) can originate from the surface source,  $^{210}\text{Pb}$ . The most intense lines are 30.1 keV (52% per decay) and 43.3 keV (13.6% per decay). There are peaks in spectra 1 and 2 at  $\sim 28$  and  $\sim 41$  keV that could be associated with these lines. All the events of these peaks should be single-point ones. The observed shift of maximum

energy with respect to the expected line could be explained by the deposit of a portion of near-wall primary ionization electrons on the cathode owing to their diffusion. With the emission of conversion electrons the residual excitation of the  $^{210}\text{Bi}$  daughter shell deenergizes by radiation of characteristic photons of  $L$  series ( $E_{L\alpha} = 10.8$  keV, 9.3% per decay;  $E_{L\beta} = 13.0$  keV, 11.2% per decay, etc.) or/and by Auger electrons. In different combinations this radiation can enter the fiducial volume simultaneously with  $\beta$  particles and c.e. In the simplest case, when c.e. with 30.2 keV and characteristic  $L\alpha$ -photon are registered, a two-point event with an energy deposit of  $\sim 42.5$  keV is produced in the gas. The fraction of such events is small enough in the total spectrum. There is a step at  $\sim 34$  keV [Figs. 5(a) and 5(b)] corresponding to the escape peak of 46.5 keV line for krypton ( $E_\gamma - E_{K_{\alpha\text{Kr}}} = 46.5 - 12.6 = 33.9$  keV).

The deviation of the shape of spectrum 1 at energies below  $\sim 50$  keV from the smooth descending substrate typical of peak energies above 50 keV can generally be attributed to the  $^{210}\text{Pb}$  source.

The scenario described above is confirmed by the distribution of events related to different peaks in the amplitude spectra, composed separately of events with different numbers of point ionization clusters in the composite pulse [23]. In Fig. 5 one can see the corresponding spectra of amplitude  $M1$  plotted after selecting the type of events by analyzing the form of electric current pulses purified from noise: (b) single-point, (c) two-point, and (d) three-point.

Comparison of the obtained relation of peak areas (13.5 and 46.5 keV) for different components with estimated values allows one to determine the efficiency,  $\varepsilon_k$ , of the procedure of the computer event selection with a given number of ionization regions. The efficiencies,  $\varepsilon_k$ , of two-point event selection were found to be 0.567 and 0.733, respectively, which are in good agreement with calculated model values: 0.604 and 0.745 [23].

As seen from Fig. 5(b), the main difference for background spectra for the LPC filled with different gases is in single-point (event) spectra. The LPC background spectra with various gases are in good agreement with each other for two- and three-point events in the energy region of 20–80 keV. For further analysis the three-point event spectra, Fig. 5(d), have been used. Each event of these spectra is characterized by a set of energy deposits distributed over three pointlike regions of the operating volume of the counter. Energy deposits are proportional to the Gaussian areas ( $G_1, G_2, G_3$ ), which describe three pointwise components of the total composite current pulse of primary ionization electrons on the border of the gas amplification region. Gaussian numbering corresponds to the arrival time sequence of the components coming into the gas amplification region. To simplify the selection of events with a given set of features the amplitudes of components for each event are arranged in the increasing order [ $(G_1, G_2, G_3) \rightarrow (q_0 \leq q_1 \leq q_2)$ ].

In the sought-for events the minimal amplitude value (two groups of Auger electrons from residual excitation with energies  $E_1 \sim 1.5$  keV and  $E_2 \sim 2.9$  keV) will correspond to the condition  $0.9$  keV  $\leq q_0 \leq 4.5$  keV: “C1”. The middle and highest amplitudes are produced by characteristic  $K$  photons

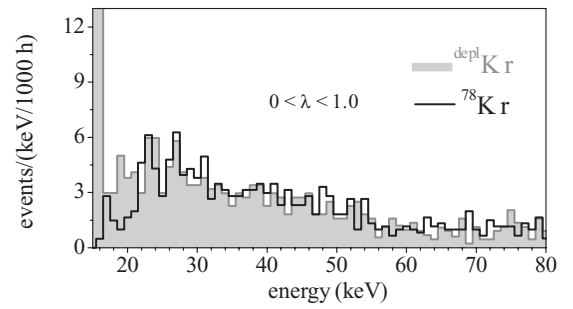


FIG. 6. The three-point spectra selected under the conditions “C1” and “C2”.

( $K_{\alpha 1} + K_{\alpha 1}, K_{\alpha 1} + K_{\alpha 2}, K_{\alpha 2} + K_{\alpha 2}, K_{\alpha 1} + K_{\beta 1}, K_{\alpha 1} + K_{\beta 2}, K_{\alpha 2} + K_{\beta 1}, K_{\alpha 2} + K_{\beta 2}$ )  $\text{Se}^{**}$ . In the total number of possible combinations, the fraction of the enumerated combinations of the two photons ( $\alpha_k$ ), registered in a composition of three-point event, is  $\alpha_k = 0.985$ . It is convenient to introduce a parameter of average to maximum amplitude ratio. With an allowance for resolution, a significant part of the event would have this parameter within  $1.0 \geq q_1/q_2 \geq 0.7$ : “C2”. The selection of events from spectra in Fig. 5(d) corresponding to the conditions (C1 and C2) allows an additional decrease in the background of the expected peak energy region.

The selected spectra are plotted in Fig. 6. They show that there are similar peaks for both spectra in the energy region of  $\sim 26$  keV corresponding to the sought-for effect. To find their nature the study of the distribution of the number of background events of various types along the anode wire has been performed. This distribution was plotted using the dependence of the relative amplitude of the first after-pulse on the distance between the point of origin of the main pulse and the middle point of the length of the anode wire. This distance defines the solid angle viewing the inner surface of the copper cathode cylinder. The solid angle through which the operating surface of the cathode is viewed from the middle point of the anode wire and from the end points of the operating length of the anode wire are  $\sim 3.9\pi$  and  $\sim 2\pi$ , respectively [Fig. 7(a)]. The density of distribution of the solid angle for the points uniformly distributed along the anode wire is presented in Fig. 7(b). There is a dependence on the solid angle of the relative number of photoelectrons, knocked out of the copper surface by the photons produced in the gas ionization. First after-pulse is produced as a consequence of gas amplification of secondary photoelectrons generated on the cathode within the operating length of the anode wire. It is the  $\lambda$  parameter [Eq. (4)], accurate to the precision set by energy resolution of pulse and after-pulse, that determines the coordinate of the primary event with respect to the middle point of the anode wire. To calibrate the counter with respect to  $\lambda$  one needs a radioactive source uniformly distributed over the LPC volume. The nuclide of  $^{81}\text{Kr}$  is well suited for this task.

A normalized distribution of the number of events of 11.5–15.5 keV energy ( $^{81}\text{Kr}$ ) from the spectrum of one-point events of the LPC background with depleted krypton versus parameter  $\lambda$  is given in Fig. 8(a) as a histogram with its maximum at  $\lambda = 0.28$ . Distribution of the number of events

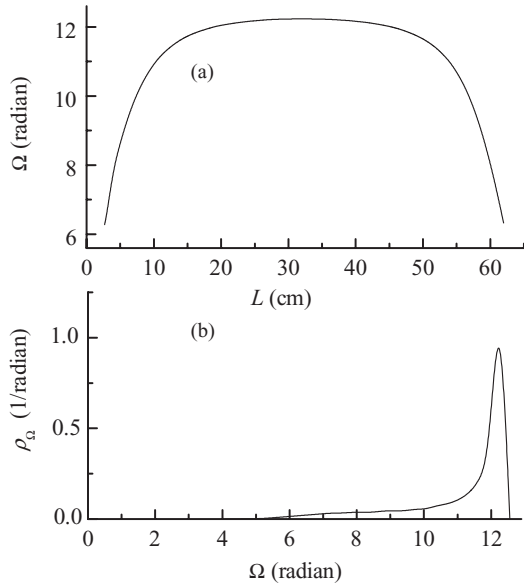


FIG. 7. (a) The solid angle under which the interior surface of the counter from different points of an anode wire is visible. (b) The density of distribution of the solid angle for the points uniformly distributed along the anode wire.

with 20–80 keV energy range is given in the same figure in the shaded region.

Comparison of the distributions shows an excess of events over a bar graph in the region of  $\lambda < 0.225$  value, corresponding to the ends of the anode wire. The form of distribution of this excess is obtained by fitting the subtracted-out histogram [“shaded region” minus “histogram”] and is presented by a dash-dotted curve. Hence, it follows that at the ends of the operating length of the anode wire there is an extra background source additional to the one that is uniformly distributed over the volume. In Figs. 8(b) and 8(c), there is similar distribution of the number of two-point and three-point events with energy 20–80 keV (shaded region) and their uniform and near-boundary components (dotted and dash-dotted curves). It is clear that the relative contribution of near-boundary into the corresponding spectrum increases with the increase of the number of pointlike ionization clusters in a given event.

The additional events at the ends of the operating length of the anode wire are produced by particles coming out of the “dead” near-end volumes of a krypton gas. Apart from the proportionally amplified components, a total pulse could also be composed of components of larger energy deposits that occur in the dead volume and are collected in the ionization mode at the end bulbs of the anode. Specifically, the  $\sim 26$  keV in spectra of Fig. 9(a) could well be formed by  $\alpha$  particles emitted from the surface of the cathode in the near-end region where the anode wire is thickened with copper tubules. An  $\alpha$  particle can ionize  $K$  shells of krypton atoms, and in this case the characteristic photons would have energies of 12.6 keV. These photons can penetrate into the operating volume of the LPC where gas amplification occurs. Registration of two photons gives two points. The third point is produced by ionization of an  $\alpha$  particle collected in the ionization mode. Discarding pulses with  $\lambda < 0.225$  one can completely eliminate such

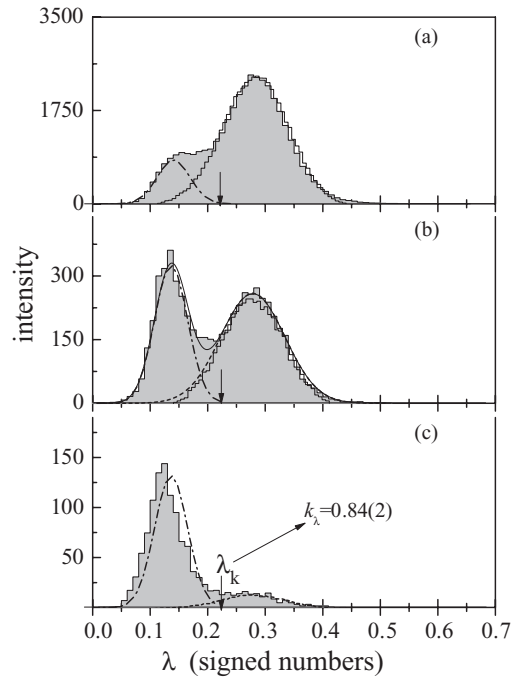


FIG. 8. The distributions of the events in the LPC filled with depleted krypton with energies 11.5–15.5 keV ( $^{81}\text{Kr}$ , black histogram) and with energies 20–80 keV (shaded region). The dash-dotted and dotted curves are the result of a fitting operation of the shaded region. (a) Single-point events, (b) two-point events, and (c) three-point events.

events from three-point spectra. The selection coefficient of useful event ( $k_\lambda$ ) remains high enough:  $k_\lambda = 0.84(2)$ .

In Fig. 9 the linear bar ( $^{78}\text{Kr}$ ) and shaded-to-zero bar graph ( $^{\text{depl}}\text{Kr}$ ) are three-point spectra selected under condition of  $\lambda \geq 0.225$  from spectra shown in Fig. 6.

To determine the value of energy release owing to  $2K$  capture in  $^{78}\text{Kr}$  the theoretical model has been developed describing the filling of  $2K$  vacancy with electrons from the upper shells [41]. Values of radiative width, atomic energies, and probability of  $ECEC$  capture are calculated in the framework of the Dirac-Fock method, using the code package RAINE [42,43]. According to Ref. [41] in case when both electron transitions are accompanied with characteristic x-ray emission, the first x-ray ( $K^{-2} \rightarrow K^{-1}L^{-1}$  or  $K^{-2} \rightarrow K^{-1}M^{-1}$  hypersatellite) energy turned out to be  $\sim 11.56$  or

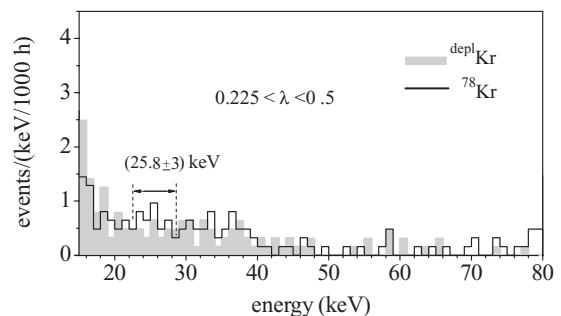


FIG. 9. The three-point spectra selected under the conditions (C1 and C2) and  $\lambda \geq 0.225$ .

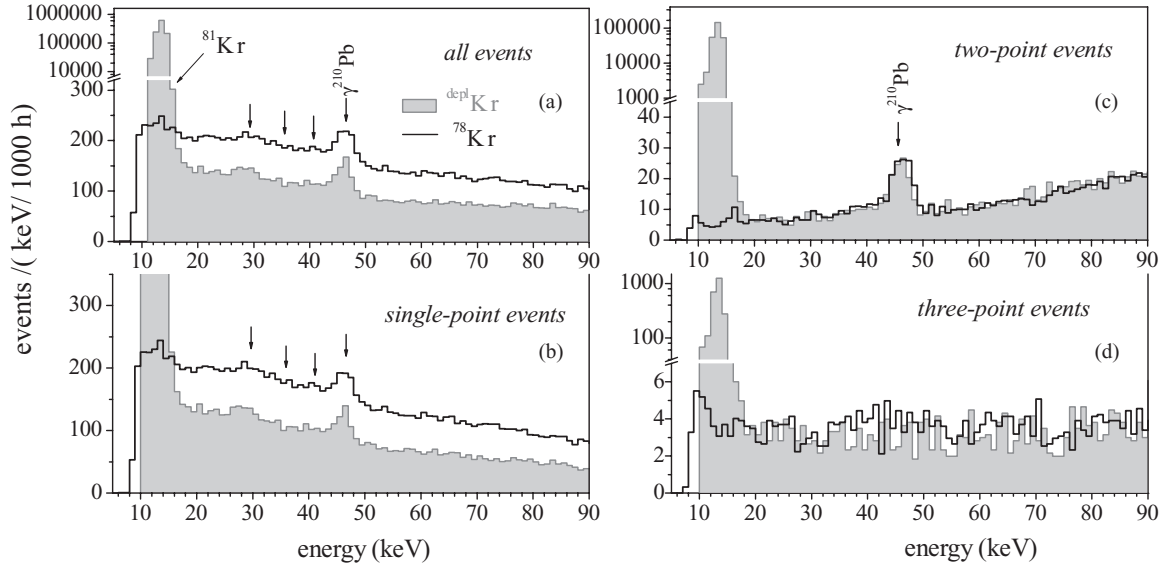


FIG. 10. Pulse height  $M1$  spectra (data of the second stage of measurements normalized for 1000 h) of the background of the LPC filled with krypton enriched in  $^{78}\text{Kr}$  (black line) and with depleted krypton (gray bar graph). (a) All events, (b) single-point events, (c), two-point events, and (d) three-point events.

$\sim 12.97$  keV. The second x-ray ( $K^{1-L^{-1}} \rightarrow L^{-2}$  satellite) energy turned out to be more than the  $K_{\alpha\beta}$  x-ray energy for single  $K$  vacancy, though only by  $\sim 50$  eV. Therefore, the total energy release is 25.8 keV. The theoretical probability of radiation of the two characteristic photons was found to be 0.47.

The background in energy region from 22.8 to 28.8 keV in spectra of Fig. 9 is  $n_1 = (38.1 \pm 6.3) \text{ y}^{-1}$  and  $n_2 = (20.7 \pm 6.0) \text{ y}^{-1}$ , respectively, which gives count rate of  $2K$  capture for  $^{78}\text{Kr}$  to be  $n_{\text{exp}} = n_1 - n_2 = (17.4 \pm 8.7) \text{ y}^{-1}$ . The obtained positive value does not exceed two standard deviations and in this case limit to the expected effect only was set for 90% C.L.:  $n_{\text{exp}} \leq 31.7 \text{ y}^{-1}$ .

The half-life limit has been calculated using formula

$$\lim T_{1/2} = \ln 2 \cdot N \cdot \frac{p_3 \cdot \varepsilon_p \cdot \varepsilon_3 \cdot \alpha_k \cdot k_\lambda}{\lim(n_{\text{exp}})}, \quad (13)$$

where  $N = 1.08 \times 10^{24}$  is the number of  $^{78}\text{Kr}$  atoms in the operating volume of the counter,  $p_3 = 0.47$  is the fraction of  $2K$  captures accompanied by the emission of two  $K$  x rays;  $\varepsilon_p = 0.81 \pm 0.01$  is the probability of two  $K$  photons to be absorbed in the operating volume;  $\varepsilon_3 = 0.5 \pm 0.05$  is the efficiency to select three-point events owing to  $2K$  capture in  $^{78}\text{Kr}$ ;  $\alpha_k = 0.985 \pm 0.005$  is the fraction of events with two  $K$  photons that could be registered as distinct three-point events;  $k_\lambda = 0.84 \pm 0.02$  is the useful event selection coefficient for a given threshold for  $\lambda$  [Fig. 8(c)]. The result obtained is

$$T_{1/2}^{2\nu 2K} (\text{g.s.} \rightarrow \text{g.s.}) \geq 3.7 \times 10^{21} \text{ y} (90\% \text{ C.L.}).$$

## VI. SECOND-STAGE MEASUREMENT RESULTS FROM THE LPC

In the second stage, inner surface of counter's casing was shielded with M0k copper, characterized by reduced amount

of radioactive admixtures. This shielding was made as a tightly adjusted set of ring plugs ( $\sim 137$  mm inner diameter) made of a copper strip (1.5 mm thick and 20 mm wide). A layer of copper of 1.5 mm thickness completely absorbs electrons escaping from the counter casing with energies up to  $\sim 1.6$  MeV. Such an update of the setup led to reduction of the background owing to  $\alpha$  particles by  $\sim 20$  times. The background in the energy range from 10 to 100 keV was reduced by  $\sim 7$  times. The positive effect of this copper layer led us to add two layers of M0k-copper (3 mm thick) mounted on the inner surface of the flanges. The total volume between the flanges became 10.3 L, and the operating volume between the ends of the anode wire caps became 8.77 L. The counter was filled with working gases to the pressure of 4.609 bar, and the amount of krypton atoms in the operating volume remained practically the same.

Figure 10 presents amplitude spectra, normalized for 1000 h, for the LPC background with enriched krypton (dark lines, total measurement time 9457 h), and with depleted krypton (light bar graph, total measurement time 6243 h). Panels (a)–(d) show spectra of (a) all recorded events, (b) single-point events, (c) two-point events, and (d) three-point events. In spectra in panels (a), (b), and (c) one can see the background  $\gamma$  line of 46.5 keV owing to the decay of isotope  $^{210}\text{Pb}$ , which is present on the surfaces of the internal parts of the counter.

Figure 10 demonstrates that spectrometric properties of the detector have not changed. However,  $\lambda$  distribution [Eq. (4)] is shifted to  $\sim 30\%$  in relation to  $\lambda$  distribution at the first stage (Fig. 8). Figure 11 shows  $\lambda$  distribution of three-point events for the background measurements of the LPC filled with krypton enriched in  $^{78}\text{Kr}$  (black curve) and with depleted krypton (gray bar graph) in the second stage. The spectra of three-point events that are selected by the next terms: (1)  $C1 \equiv 0.89 \leq q_0 \leq 4.5$  keV; (2)  $C2 \equiv 1.0 \geq q_1/q_2 \geq 0.7$ ; (3)  $\lambda > 0.155$  are shown in Fig. 12 for both samples. In the

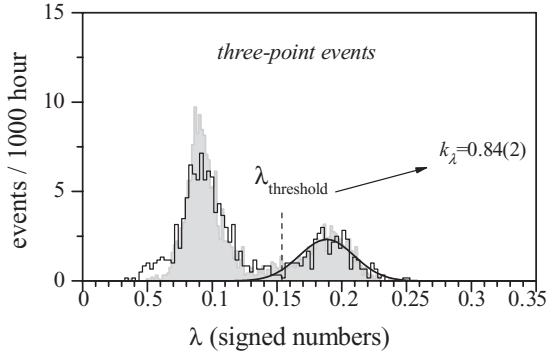


FIG. 11.  $\lambda$  distributions of three-point events in the LPC filled with krypton enriched in  $^{78}\text{Kr}$  (black line) and with depleted krypton (gray bar graph).

same figure the model spectrum from  $2K$  capture is given. One can see that in the spectrum of the enriched sample there is an excess of events in the region of expected effect. The background in the spectrum of enriched and depleted krypton in the energy range from 22.8 to 28.8 keV was found to be  $N_1 = 15$  for 9457 h and  $N_2 = 4$  for 6243 h ( $\sim 6$  in 9457 h), respectively. For the values of (effect + background) = 15 and background = 6, it follows from recommendations of Ref. [44] that for the confidence level of 90% the effect for 9457 h is equal to  $N_{\text{exp}} = 9.0^{+7.52}_{-5.52}$  or  $n_{\text{exp}} = 8.3^{+7.0}_{-5.1} \text{ y}^{-1}$ . Statistical significance of the excess is relatively low ( $\sim 2\sigma$ ) and could only be interpreted as a possible indication of effect. Assuming this effect being attributable to  $2\nu 2K$  capture in  $^{78}\text{Kr}$ , one can estimate the half-life for this process. Using the above formula (13) the half-life was found to be

$$T_{1/2}^{2\nu 2K}(\text{g.s.} \rightarrow \text{g.s.}) = [1.4^{+2.3}_{-0.7}(\text{stat}) \pm 0.2(\text{syst})] \times 10^{22} \text{y}$$

or conservative value would be

$$T_{1/2}^{2\nu 2K}(\text{g.s.} \rightarrow \text{g.s.}) \geq 7.7 \times 10^{21} \text{y} \text{ (90\%C.L.)},$$

where the systematic error is defined as uncertainty factors in Eq. (13).

The presence of a peak in the region of interest in the enriched sample allows us to apply an alternative approach

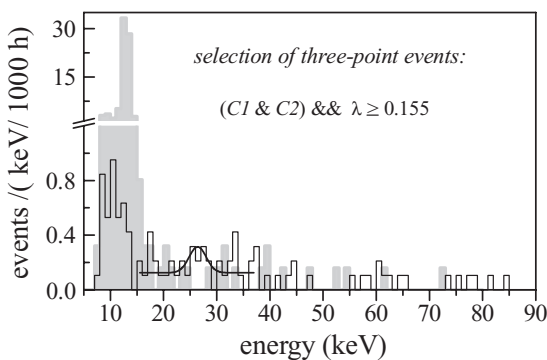


FIG. 12. The three-point spectra selected under the conditions (C1 and C2) and  $\lambda \geq 0.155$ : krypton enriched in  $^{78}\text{Kr}$  (black line), depleted krypton (gray bar graph), and model calculation spectrum for  $2K$  capture.

which does not consider the depleted spectrum and gives the following data: (effect + background) = 15 and (the background average substrate) = 8. The effect is equal to  $N_{\text{exp}} = 6.6^{+6.3}_{-4.3} \text{ y}^{-1}$  following the recommendations [44] for the confidence level of 90%. It gives a less conservative result,

$$T_{1/2}^{2\nu 2K}(\text{g.s.} \rightarrow \text{g.s.}) = [1.8^{+4.4}_{-0.9}(\text{stat}) \pm 0.2(\text{syst})] \times 10^{22} \text{y};$$

its conservative value would be

$$T_{1/2}^{2\nu 2K}(\text{g.s.} \rightarrow \text{g.s.}) \geq 8.7 \times 10^{21} \text{y} \text{ (90\%C.L.)}.$$

## VII. THE COMBINED RESULT

To increase the statistical significance of the observed in both series excess of events, which could be attributed to the effect under study, their results were combined. Average annual count rates have been summed and then normalized to 1 y.

The following count rates of background were obtained  $n_1 = 26.0^{+3.8}_{-3.6} \text{ y}^{-1}$  and  $n_2 = 13.2^{+3.6}_{-3.2} \text{ y}^{-1}$ , giving the count rate of  $2\nu 2K$ -capture events in  $^{78}\text{Kr}$  equal to  $n_{\text{exp}} = n_1 - n_2 = 12.8^{+5.2}_{-4.8} \text{ y}^{-1}$ . Statistical significance of this result is  $\sim 2.5\sigma$ . At a confidence level of 90% the half-life was found to be

$$T_{1/2}^{2\nu 2K}(\text{g.s.} \rightarrow \text{g.s.}) = [9.2^{+5.5}_{-2.6}(\text{stat}) \pm 1.3(\text{syst})] \times 10^{21} \text{y},$$

with a conservative value

$$T_{1/2}^{2\nu 2K}(\text{g.s.} \rightarrow \text{g.s.}) \geq 5.5 \times 10^{21} \text{y}.$$

Apart from  $2\nu 2K$  capture to the ground level of a daughter nucleus of  $^{78}\text{Se}$ , three-point events with specified parameters could be attributable to the following captures:  $2\nu 2K$  capture to the excited level  $0_1^+$  (1498.599 keV [45]), to resonance  $0\nu 2K$  capture to the excited level  $2^+$  (2838.49 keV [45]), and to  $0\nu 2K$  capture on the ground level. Apparently from Table II, the input of each of these possible processes to the total amount of useful three-point events does not exceed a tenths fractions of 1% from the input of  $2\nu 2K$  capture to the ground level of  $^{78}\text{Se}$ . Therefore, the total excess of events given above, within achieved statistical accuracy, was attributed to the latter process only.

The predicted half-life for the ( $2\nu 2K; 0^+ \rightarrow 0_1^+$ ) transition is  $3.7 \times 10^{24} \text{ y}$  [12]. The level deexcites by emitting cascade photons of 884.8- and 613.6-keV energies [45]. The total efficiency of both photons interaction with krypton in the operating volume of the counter is 0.025, according to calculations using packages of GEANT-4. Such interaction gives rise to additional energy release in one or two points of the operating volume and excludes the event from the number of useful ones. Taking this into account, the efficiency of registration of ( $2\nu 2K; 0^+ \rightarrow 0_1^+$ ) transition was found to be  $\varepsilon_b = 0.975$ . One can attribute the obtained maximum possible value (at 90% C.L.) of the measured effect ( $12.8 + 1.64 \times 5.2 = 21.3$ )  $\text{y}^{-1}$  to the process under study. Taking into account the value of  $\varepsilon_b$  the lower limit to half-life for  $^{78}\text{Kr}$  for this transition was found to be

$$T_{1/2}^{2\nu 2K}(\text{g.s.} \rightarrow 1498.6\text{keV}) \geq 5.4 \times 10^{21} \text{y}.$$

To register the transition to the excited levels a proportional counter should be surrounded by effective detectors of  $\gamma$

TABLE II. Experimental limits (or values) and theoretical estimates of half-lives for various  $\beta\beta$  processes in the transition of  $^{78}\text{Kr} \rightarrow ^{78}\text{Se}$ .  $T_{1/2}$  limits are derived in the present work and Ref. [22] at 90% C.L., while those from Ref. [51] are at 68% C.L. The range given in parentheses for the theoretical estimations of the half-life is given for  $g_A/g_V = 1.261$  and 1, respectively.

Transition		Final level of $^{78}\text{Se}$	$T_{1/2}$ (y)			
Decay channel	Decay mode		Experiment		Theoretical estimations	
			Present work	Other works		
<i>ECEC</i>	$2\nu$	$0_{\text{g.s.}}^+$	–	–	MCM	$(0.37-0.94) \times 10^{22}$ [12]
					MCM	$(0.82-6.80) \times 10^{22}$ [13]
					QRPA	$(3.70-9.40) \times 10^{22}$ [14]
					$\text{SU}(4)_{\sigma\tau}$	$(62-156.77) \times 10^{22}$ [15]
					DSM	$(2.11-5.33) \times 10^{22}$ [11]
$2K$	$2\nu$	$0_1^+, 1499 \text{ keV}$	–	–	MCM	$3.7 \times 10^{24}$ [12]
			$\approx 9.2_{-2.6}^{+5.5} \times 10^{21}$	$\geq 2.3 \times 10^{20}$ [22]	MCM <sup>a</sup>	$(4.7-12) \times 10^{21}$ [12]
			$\geq 5.4 \times 10^{21}$	–	MCM <sup>a</sup>	$4.7 \times 10^{24}$ [12]
$2K\gamma_b$	$0\nu$	$0_{\text{g.s.}}^+$	$\geq 5.5 \times 10^{21}$	–	–	–
$2K$	$0\nu$	$2^+, 2838 \text{ keV}$	$\geq 5.4 \times 10^{21}$	–	–	–
$K\beta^+$	$2\nu$	$0_{\text{g.s.}}^+$	–	$\geq 1.1 \times 10^{20}$ [51]	MCM	$6.2 \times 10^{21}$ [12]
					$\text{SU}(4)_{\sigma\tau}$	$1.0 \times 10^{24}$ [15]
$K\beta^+$	$0\nu$	$0_{\text{g.s.}}^+$	–	$\geq 5.1 \times 10^{21}$ [51]	–	–
$\beta^+\beta^+$	$2\nu$	$0_{\text{g.s.}}^+$	–	$\geq 2.0 \times 10^{21}$ [51]	–	–
$\beta^+\beta^+$	$0\nu$	$0_{\text{g.s.}}^+$	–	$\geq 2.0 \times 10^{21}$ [51]	–	–

<sup>a</sup>The fraction of  $2\nu 2K$ -capture events in  $^{78}\text{Kr}$  with respect to the total number of  $2\nu ECEC$ -capture events is 78.6% [16].

rays, for example, with a layer of NaI(Tl) crystals. The data obtained in our experiment make it possible to estimate of sensitivity  $S$  of such an experiment. We assume the efficiency of  $\gamma$  registration to be not worse than  $\varepsilon_\gamma = 0.5$ . If during 1 y of measurements with described enriched sample there would be no coincidence of useful three-point events with signals, specified in energy, from the  $\gamma$  detector, then, according to Ref. [44], with zero values of a background and signal, the effect by 90% C.L. does not exceed  $2.44 \text{ y}^{-1}$ . Using Eq. (13) and taking  $\varepsilon_\gamma$  into account, one can estimate the sensitivity for the half-life of 1 y of measurement  $S = 2.4 \times 10^{22} \text{ y}$  (at 90% C.L.).

The general characteristics of the resonance  $0\nu 2K$  capture to the excited level are considered in Ref. [46]. This process occurs under the condition of  $Q^*(2K) = \Delta M - E^* - 2E_{K_{ab}} \approx 0$  ( $< 0.1$ ) keV, where  $\Delta M$  is the mass difference between mother and daughter atoms;  $E^*$  is the energy of the appropriate excited level of the daughter nucleus;  $E_{K_{ab}}$  is the binding energy of a  $K$  electron in a daughter atom;  $Q^*(2K)$  is the energy balance. This condition fulfilled the probability of the process increases by  $10^4-10^6$  times with regard to the transition to the ground level. The resonance transition for  $^{78}\text{Kr}$  was treated in Ref. [47], but calculating the energy balance for this process one has to take into account that  $2E_{K_{ab}} = 25.8 \text{ keV}$  for the daughter nuclei of selenium.

Theoretical estimations of  $\Delta M$  in various approaches lay in the range of 2650–2900 keV [48]. Two values of  $\Delta M$  are taken from two databases of atomic mass evaluation: (1)  $2846.4 \pm 2.0 \text{ keV}$  [49]; (2)  $2866 \pm 7 \text{ keV}$  [50]. For the first value, energy balance  $Q^*(2K) = (2846.4 \pm 2.0) - 2838.49 - 25.8 = (-17.89 \pm 2.0) \text{ keV}$  does not satisfy the resonant conditions. For the second value  $Q^*(2K) = (2866 \pm 7.0) - 2838.49 -$

$25.8 = (1.71 \pm 7.0) \text{ keV}$ , and there is probability that with  $\Delta M$ 's uncertainty the condition for the resonance transition is fulfilled. The effect obtained above allows one to set a limit to this transition.

The excited level deexcites in cascade transitions by  $\gamma$ -ray emission in different combinations. The most probable combinations are: (1)  $[1530.0 + 694.8(63\%) + 613.6 \text{ keV}, 1530.0 + 1308.6(37\%); 41\%]$ ; (2)  $[1080.0 + 1144.8 + 613.6 \text{ keV}; 31\%]$  [45]. Using these combinations of  $\gamma$  rays the efficiencies of interaction have been calculated and the total efficiency normalized to 100% was found to be 0.033. Using this value, the probability to register such a process as a standard three-point event was found to be  $\varepsilon_b = 0.967$ . Therefore, the lower limit to the half-life of  $^{78}\text{Kr}$  with regard to resonance  $0\nu 2K$  capture to the excited level is

$$T_{1/2}^{0\nu 2K}(\text{g.s.} \rightarrow 2838\text{keV}) \geq 5.4 \times 10^{21} \text{ y (90\% C.L.)}$$

The consideration presented above has illustrated clearly the necessity to obtain more accurate data on  $\Delta M$  to make a final conclusion about the possibility of this type of transition.

If one assumes that the observed effect, in spite of the relatively low statistical significance, is truly that of  $2\nu 2K$  capture, then, with favorable value of  $\Delta M$ , one can make an experiment to search for resonance  $0\nu 2K$  capture of  $^{78}\text{Kr}$  to the excited level with sensitivity close to the value  $S$  obtained above for  $2\nu 2K$  capture to the excited level.

The process of  $0\nu 2K$  capture to the ground state is strongly suppressed owing to nonconservation of spin [46]. When this process does take place, the excessive energy is emitted through one or several bremsstrahlung photons or an electron

positron pair. Similar events are not considered as useful ones in our technique. One can obtain a half-life limit for the case when one bremsstrahlung photon is emitted. The energy of a bremsstrahlung photon ( $\gamma_b$ ) is equal to the total transition energy minus the doubled value of the electron binding energy in the  $K$  shell of selenium. Taking the above considerations into account one obtains  $E_{\gamma_b} \approx 2840$  keV. The efficiency of interactions for such quanta in the working gas is 0.01. The probability to register three-point events is  $\varepsilon_{\gamma_b} = 0.99$ , and in such a case

$$T_{1/2}^{0\nu 2K \gamma_b}(\text{g.s.} \rightarrow \text{g.s.}) \geq 5.5 \times 10^{21} \text{y} \text{ (90\%C.L.)}.$$

### VIII. CONCLUSION

In the consideration above the possibility to reduce the proportional counter background by  $\sim 2000$  times in registering the process of  $2K$  capture in  $^{78}\text{Kr}$  by selecting useful pulses according to the amount of pointwise like clusters and coordinate of the event on the anode wire has been demonstrated. The results of two independent series of measurements with different intrinsic background of a copper proportional counter have been presented. In both series of measurements the selected spectra of three-point events from the LPC filled with enriched krypton show the excess of events in the region under study. The observed excess does not exceed two standard deviations. The statistical significance of the excess of the combined data set is  $\sim 2.5\sigma$ . If the observed effect is attributable to  $2\nu 2K$  capture in  $^{78}\text{Kr}$ , then the appropriate value of the half-life is

$$T_{1/2}^{2\nu 2K} = [9.2_{-2.6}^{+5.5}(\text{stat}) \pm 1.3(\text{syst})] \times 10^{21} \text{y} \text{ (90\%C.L.)},$$

or, conservatively,

$$T_{1/2}^{2\nu 2K} \geq 5.5 \times 10^{21} \text{y} \text{ (90\%C.L.)}.$$

From the combined data for two series of measurements the limits to half-life with regard to other  $2K$  capture modes have been obtained (all the limits are at 90% C.L.):

- (1)  $2\nu 2K$  capture to the excited level  $0_1^+$  (1498.599 keV),

$$T_{1/2}^{2\nu 2K}(0^+ \rightarrow 0_1^+) \geq 5.4 \times 10^{21} \text{y};$$

- (2) close to the resonance  $2(0\nu)$  capture to the excited level  $2^+$  (2838.49 keV),

$$T_{1/2}^{0\nu 2K}(0^+ \rightarrow 2^+) \geq 5.4 \times 10^{21} \text{y};$$

- (3)  $0\nu 2K$  capture to the ground level,

$$T_{1/2}^{0\nu 2K \gamma_b}(0^+ \rightarrow 0^+) \geq 5.5 \times 10^{21} \text{y}.$$

All results of experimental search of double- $\beta$  processes in  $^{78}\text{Kr}$  obtained in the present work are summarized in Table II. Results of the most sensitive previous experiments and theoretical estimates are given for comparison also.

### ACKNOWLEDGMENTS

We are very thankful to Professor V. N. Gavrin for allocation of the experimental equipment in the underground laboratory of the Gallium Germanium Neutrino Telescope and also for his contribution in the early stages of this work. The authors are grateful to Dr. Boris Pritychenko and Dr. Timothy Johnson for productive discussions and careful reading of the manuscript and useful suggestions, respectively. We would like to thank Professor A. S. Barabash for his useful remarks. This work was supported by the Russian Foundation for Basic Research (Grant No. 04-02-16037) and also by the Neutrino Physics Program (2006-2009) and the Neutrino Physics and Neutrino Astrophysics Program (2009-2011) of the Presidium of the Russian Academy of Sciences.

- 
- [1] A. S. Barabash, *Phys. Rev. C* **81**, 035501 (2010).  
 [2] N. Ackerman *et al.* (EXO Collaboration), *Phys. Rev. Lett.* **107**, 212501 (2011).  
 [3] A. Gando *et al.* (KamLAND-Zen Collaboration), *Phys. Rev. C* **85**, 045504 (2012).  
 [4] A. S. Barabash *et al.*, *Phys. Atomic Nuclei* **73**, 162 (2010).  
 [5] A. S. Barabash *et al.*, *Phys. Rev. C* **83**, 045503 (2011).  
 [6] P. Belli *et al.*, *J. Phys. (London)* **G38**, 015103 (2011); *Eur. Phys. J. A* **47**, 91 (2011); *J. Phys. (London)* **G38**, 115107 (2011).  
 [7] N. I. Rukhadze *et al.*, *Nucl. Phys. A* **852**, 197 (2011).  
 [8] P. Belli *et al.*, *Phys. Rev. C* **85**, 044610 (2012).  
 [9] A. P. Meshik, C. M. Hohenberg, O. V. Pravdivtseva, and Y. S. Kapusta, *Phys. Rev. C* **64**, 035205 (2001).  
 [10] Ju. M. Gavriljuk *et al.*, *Phys. At. Nucl.* **69**, 2124 (2006).  
 [11] S. Mishra, A. Shukla, R. Sahu, and V. K. B. Kota, *Phys. Rev. C* **78**, 024307 (2008).  
 [12] M. Aunola and J. Suchonen, *Nucl. Phys. A* **602**, 133 (1996).  
 [13] J. Toivanen and J. Suhonen, *Phys. Rev. C* **55**, 2314 (1997).  
 [14] M. Hirsch *et al.*, *Z. Phys. A* **347**, 151 (1994).  
 [15] O. Romyantsev and M. Urin, *Phys. Lett. B* **443**, 51 (1998).  
 [16] M. Doi and T. Kotani, *Prog. Theor. Phys.* **87**, 1207 (1992).  
 [17] A. C. Thompson (ed.), *X-Ray Data Booklet* (Center for X-ray Optics and Advanced Light Source, LBNL, Berkeley, CA, 2009), <http://www.scribd.com/doc/>; <http://xdb.lbl.gov>  
 [18] E. Storm and H. I. Israel, *Atom. Data Nucl. Data Tables* **7**, 565 (1970).  
 [19] A. Peisert and F. Sauli, *Drift and Diffusion of Electrons in Gases: A Compilation*, preprint CERN 84-08, 13 July, 1984.  
 [20] V. N. Gavrin *et al.*, preprint INR RAN, P-698, Moscow, 1991.  
 [21] A. N. Shubin *et al.*, in *Proceedings of the VII International Scientific Conference: Physical and Chemical Processes on Selection of Atoms and Molecules, Zvenigorod, October 6–10, 2003* (Atominform, Moscow, 2003).  
 [22] Ju. M. Gavriljuk *et al.*, *Phys. Atomic Nuclei* **63**, 2201 (2000).  
 [23] Yu. M. Gavriljuk *et al.*, *Instrum. Exp. Tech.* **53**, 57 (2010).  
 [24] S. S. Ratkevich, *Vis. Khar. Nat. Univ.* **746**, 23 (2006).  
 [25] I. Daubechies, *Ten Lectures on Wavelets* (SIAM, Philadelphia, 1992).  
 [26] J. C. van den Berg (ed.), *Wavelets in Physics* (Cambridge University Press, Cambridge, UK, 1999).  
 [27] S. Mallat, *IEEE Trans. Pat. Anal. Mach. Intell.* **11**, 674 (1989).  
 [28] B. M. Kessler, G. L. Payne, and W. N. Polyzoou, *Phys. Rev. C* **70**, 034003 (2004).

- [29] Fatih Bulut and W. N. Polyzou, *Phys. Rev. C* **73**, 024003 (2006).
- [30] S. Mallat, *A Wavelet Tour of Signal Processing* (Academic Press, New York, 1998).
- [31] D. L. Donoho and I. M. Johnstone, *J. Am. Stat. Assoc.* **90**, 1200 (1995).
- [32] M. Neumann and R. Sachs, *Ann. Stat.* **25**, 38 (1997).
- [33] C. M. Stein, *Ann. Stat.* **9**, 1135 (1981).
- [34] L. Birgé and P. Massart, in *From Model Selection to Adaptive Estimation*, edited by D. Pollard (Festschrift for L. Le Cam, Springer, Berlin, 1997).
- [35] <http://www.mathworks.com/products/wavelet/>
- [36] D. L. Donoho, Technical Report, Department of Statistics, Stanford University, 1992.
- [37] Evaluated Nuclear Structure Data File (ENSDF), <http://www.nndc.bnl.gov/ensdf>
- [38] H. H. Loosli, in *Physics and Applications*, Vol. 8 (Veda, Bratislava, 1982), p. 103.
- [39] V. V. Kuzminov and A. A. Pomansky, *Radiocarbon* **22**, 311 (1980).
- [40] W. M. Chew *et al.*, *Nucl. Phys. A* **229**, 79 (1974).
- [41] F. F. Karpeshin, M. B. Trzhaskovskaya, and V. V. Kuzminov, *Bull. Russ. Acad. Sci.: Phys.* **76**, 884 (2012).
- [42] I. M. Band, M. A. Listengarten, and M. B. Trzhaskovskaya, Leningrad Nuclear Physics Institute Report LNPI-1479, 1989.
- [43] I. M. Band and M. B. Trzhaskovskaya, *At. Data Nucl. Data Tables* **55**, 431 (1993)
- [44] G. J. Feldman and R. D. Cousins, *Phys. Rev. D* **57**, 3873 (1998).
- [45] A. R. Farhan and B. Singh, *Nucl. Data Sheets* **110**, 1917 (2009).
- [46] Z. Sujkowski and S. Wycech, *Phys. Rev. C* **70**, 052501 (2004).
- [47] A. S. Barabash, *Phys. Atom. Nucl.* **73**, 162 (2010).
- [48] *Table of Isotopes Atomic Mass*, <http://ie.lbl.gov/toimass.html>
- [49] G. Audi *et al.*, *Nucl. Phys. A* **729**, 3 (2003); *Double Beta ( $\beta\beta$ ) Decay Data* (BNL, National Nuclear Data Center), <http://www.nndc.bnl.gov/bbdecay>
- [50] G. Audi and A. H. Wapstra, *Nucl. Phys. A* **595**, 409 (1995).
- [51] C. Saenz *et al.*, *Phys. Rev. C* **50**, 1170 (1994).